Monthly Notices of the ROYAL ASTRONOMICAL SOCIETY

MNRAS **534,** 2263–2276 (2024) https://doi.org/10.1093/mnras/stae2164
Advance Access publication 2024 September 26

Modelling the impact of host galaxy dust on type Ia supernova distance measurements

B. Popovic,[1] P. Wiseman,[2★] M. Sullivan,[2] M. Smith,[3] S. González-Gaitán,[4] D. Scolnic,[1] J. Duarte,[4] P. Armstrong,[5] J. Asorey,[6] D. Brout,[7,8] D. Carollo,[9] L. Galbany,[10,11] K. Glazebrook,[7] L. Kelsey,[12] R. Kessler,[13,14] C. Lidman,[5,15] J. Lee,[16] G. F. Lewis,[17] A. Möller,[7] R. C. Nichol,[18] B. O. Sánchez,[1,19] M. Toy,[2] B. E. Tucker,[5] M. Vincenzi,[1,2] T. M. C. Abbott,[20] M. Aguena,[21] F. Andrade-Oliveira,[22] D. Bacon,[12] D. Brooks,[23] D. L. Burke,[24,25] A. Carnero Rosell,[21,26] J. Carretero,[27] F. J. Castander,[10,11] L. N. da Costa,[21] M. E. S. Pereira,[28] T. M. Davis,[29] S. Desai,[30] S. Everett,[31] I. Ferrero,[32] B. Flaugher,[33] J. García-Bellido,[34] E. Gaztanaga,[10,11,12] R. A. Gruendl,[35,36] G. Gutierrez,[33] S. R. Hinton,[29] D. L. Hollowood,[37] K. Honscheid,[38,39] D. J. James,[8] K. Kuehn,[40,41] O. Lahav,[23] S. Lee,[31] J. L. Marshall,[42] J. Mena-Fernández,[43] R. Miquel,[27,44] J. Myles,[45] R. L. C. Ogando,[46] A. Palmese,[47] A. Pieres,[21,46] A. A. Plazas Malagón,[24,25] E. Sanchez,[48] D. Sanchez Cid,[48] M. Schubnell,[49] I. Sevilla-Noarbe,[48] E. Suchyta,[50] M. E. C. Swanson,[35] G. Tarle,[49] V. Vikram,[22] and N. Weaverdyck[51] (DES Collaboration)

Affiliations are listed at the end of the paper

Accepted 2024 September 11. Received 2024 September 10; in original form 2024 June 11

ABSTRACT

Type Ia Supernovae (SNe Ia) are a critical tool in measuring the accelerating expansion of the universe. Recent efforts to improve these standard candles have focused on incorporating the effects of dust on distance measurements with SNe Ia. In this paper, we use the state-of-the-art Dark Energy Survey 5 year sample to evaluate two different families of dust models: empirical extinction models derived from SNe Ia data and physical attenuation models from the spectra of galaxies. In this work, we use realistic simulations of SNe Ia to forward-model different models of dust and compare summary statistics in order to test different assumptions and impacts on SNe Ia data. Among the SNe Ia-derived models, we find that a logistic function of the total-to-selective extinction R_V best recreates the correlations between supernova distance measurements and host galaxy properties, though an additional 0.02 mag of grey scatter is needed to fully explain the scatter in SNIa brightness in all cases. These empirically derived extinction distributions are highly incompatible with the physical attenuation models from galactic spectral measurements. From these results, we conclude that SNe Ia must either preferentially select extreme ends of galactic dust distributions, or that the characterization of dust along the SNe Ia line-of-sight is incompatible with that of galactic dust distributions.

Key words: supernovae: general – ISM: dust, extinction – cosmology: distance scale.

1 INTRODUCTION

Type Ia supernovae (SNe Ia) have been critical tools in the measurement of the accelerating expansion of the universe (Riess et al. 1998; Perlmutter et al. 1999). This accelerating expansion may be driven by 'dark energy', parametrized by an equation of state w. Despite more than two decades of investigation, the nature of dark energy remains a cosmological mystery.

To measure the accelerating expansion, the brightness of SNe Ia must be standardized in order to measure the distance to the SN (e.g. Phillips 1993; Tripp 1998). The largest standardization correction accounts for the observation that redder SNe Ia are fainter and bluer SNe Ia are brighter (the 'colour–luminosity' relation) and is based on measurements of the SN colours. This colour is likely to be a combination of an intrinsic SN colour and an extrinsic reddening due to dust along the line of sight to the SN. Some early SN Ia standardization approaches attempted to separate the intrinsic colour and dust effects (Riess, Press & Kirshner 1996; Jha, Riess & Kirshner 2007), assuming a phase-dependent intrinsic colour and an exponential distribution of dust reddening. Some modern methods also attempt the same separation (e.g. Burns et al. 2011; Mandel, Narayan & Kirshner 2011; Burns et al. 2014; Mandel et al. 2017; Thorp et al. 2021; Ward et al. 2023; Grayling et al. 2024) and tend to find that R_V is anticorrelated with the inferred total extinction A_V (dustier lines of sight have smaller R_V), with no conclusive correlations with host galaxy properties. The commonly used SALT light curve model (Guy et al. 2005, 2007) does not differentiate

★ E-mail: p.s.wiseman@soton.ac.uk

between the different astrophysical sources that affect the SN colour. Using the SALT standardization framework to measure distances with SNe Ia assumes that intrinsic colour and extrinsic dust share the same colour–luminosity standardization relationship (hereafter β).

Brout & Scolnic (2021) suggest that SNe Ia may not be affected by a common R_V – the ratio of total to selective extinction caused by dust $A_V = R_V \times E_{\rm dust}$ – across all galaxy types and environments, and therefore the standardization assumption of a universal β may not be valid (González-Gaitán et al. 2021). Instead, a variation in R_V will cause a different amount of extinction for the same amount of reddening, resulting in a different effective value of β. If these R_V differences are indeed host galaxy dependent, they may explain a number of otherwise puzzling observational effects in SN Ia data. These include (i) the so-called 'mass step', the observation that SN Ia standardized brightnesses are 0.05–0.15 mag fainter in low-mass galaxies than in high-mass galaxies (Kelly et al. 2010; Lampeitl et al. 2010; Sullivan et al. 2010), (ii) the observation that β decreases with increasing stellar mass (Sullivan et al. 2011), and (iii) the observation that the scatter in SN Ia Hubble residuals increases in SNe Ia with redder colours (Brout & Scolnic 2021). Interestingly and in contrast, recent work by Ginolin et al. (2024) using a high-completeness, low-redshift sample does not show evidence for an increasing size of mass step with redder SNe.

Without being able to measure the R_V and $E(B-V)$ of each SN in the SALT framework, Popovic et al. (2021) developed a Markov Chain Monte-Carlo technique to infer the R_V and $E(B-V)$ of SN Ia populations from their SALT parameter and Hubble residual distributions. They found a $\Delta R_V \sim -1$ between low- and high-mass galaxies is required to explain the Hubble residual versus SN colour trend. Vincenzi et al. (2024) implement this technique on the Dark Energy Survey 5-year sample of SNe Ia and find a similar ΔR_V as well as a residual mass step of 0.04 mag across all SN colours. Wiseman et al. (2022) implemented a forward-modelling of the relationship between SNe Ia and their host galaxies, tracing SN Ia progenitors through a toy model of galaxy evolution through star formation history and stellar mass. They found similar ΔR_V values to Popovic et al. (2023b), regardless of whether the R_V varies as a function of stellar mass or mass-weighted galaxy age.

These results, and the Brout & Scolnic (2021) model, find that a smaller R_V is needed in high-mass galaxies (Popovic et al. 2021, 2023b), or in galaxies with older stellar populations (Wiseman et al. 2022, 2023). In addition, the offsets between the R_V of SNe Ia in low- and high-mass galaxies are large and assumed to be a step function. Independent observational evidence for such R_V variation is scant, with most studies demonstrating any R_V variation to be in the opposite sense. For example, Salim, Boquien & Lee (2018, hereafter S18) measured dust attenuation in a large sample of star-forming and quiescent galaxies and found that amongst star-forming galaxies, the slope of the dust extinction law (R_V) *increases* as a function of stellar mass, the opposite sense to that inferred from the SN distance measurements. With specific star-formation rate (sSFR), there is a strong bimodality: low-sSFR, passive galaxies show $R_V \simeq 2.6$ whereas the mean for star-forming galaxies is 3.15, close to the average Milky Way value. This ΔR_V of $\sim$0.5 is significantly smaller than the $\sim$1 inferred from SN distance residuals by Brout & Scolnic (2021); Wiseman et al. (2022); Popovic et al. (2023b).

However, these R_V values measured by S18 and within the Milky Way may not be directly comparable to the R_V values derived from supernova measurements. Attenuation is not the same as extinction: it is the integrated effect of absorption and scattering both into and out of the line of sight to an unresolved ensemble of stars, whereas the extinction affecting an SN is purely a property of the line of sight to that SN (see Duarte et al. 2022, for an investigation into the affects of attenuation on SN hosts). The R_V along any given line of sight in a galaxy can also vary, as demonstrated by the large spread of values measured along different lines of sight to individual stars in the Milky Way (Schlafly et al. 2016) and the Magellanic Clouds (Gao et al. 2013).

The study of SNe Ia in the NIR has found conflicting evidence for differing mean R_V populations across low- and high-mass galaxies. Johansson et al. (2021), using the light-curve fitter SNooPy Burns et al. (2011), found evidence for these differing R_V values; in contrast, studies with BayeSN, from Thorp et al. (2021), Ward et al. (2023), Grayling et al. (2024), find varying, but not strong, evidence of a consistent R_V population. An additional complication is the question of whether R_V variation can capture the full diversity of the observational trends. Recent works such as Rigault et al. (2018), Rose, Garnavich & Berg (2019), Briday et al. (2022), Kelsey et al. (2022), and Wiseman et al. (2023), have shown that properties related to the age of the stellar population local to the SN explosion site show the largest difference in SN Hubble residuals. Rigault et al. (2018) and Wiseman et al. (2023) show that the local specific star formation rate (LsSFR) is an effective tracer of the delay time distributions of SNe Ia, and that this property impacts the observed light curve stretch x_1. Briday et al. (2022) and Kelsey et al. (2022), in turn, investigate the effects of local versus global environments and their impact on SNIa properties and test different 'true' sources of SNIa properties versus their observed tracer. In this paper we attempt to reconcile the ΔR_V between SN Ia sight lines in low- and high-mass galaxies inferred from the cosmological measurements to those measured in galaxy samples. We address the non-physical 'step' nature of the R_V difference and demonstrate that R_V variations cannot account for the full intrinsic scatter of SN Ia distance moduli.

In Section 2, we present the Dark Energy Survey and low-redshift supernova and host galaxy data used in this paper, followed by a review of dust models and the light-curve fitter in Section 3. The dust models that we review are presented in Section 4 and results are given in Section 5. Finally, the conclusions and discussion can be found in Section 6.

2 DATA

In this paper, we use the '5-year' data release from the Dark Energy Survey (DES; Flaugher et al. 2015) SN programme (DES-SN;Sánchez et al. 2024). This release provides 1500 likely DES SNe Ia over $0.1 < z < 1.13$ with $griz$ light curves. Host galaxies are retrieved from deep co-added images (Wiseman et al. 2020), and properties such as stellar mass and rest-frame colour are derived by fitting their spectral energy distributions with population synthesis templates (Smith et al. 2020; Kelsey et al. 2022). Each DES SN has a spectroscopic (host-galaxy) redshift from the Australian DES survey (OzDES) using the Anglo-Australian Telescope (Yuan et al. 2015; Childress et al. 2017; Lidman et al. 2020), coupled with a photometric classification using the SuperNNova program (Möller & de Boissière 2020).

The DES-SN sample is complemented with external low-redshift samples: CfA3 (Hicken et al. 2009), CfA4 (Hicken et al. 2012), CSP (Krisciunas et al. 2017) (DR3), and the Foundation SN sample (Foley et al. 2018). We use these low-z complement samples without modification. These samples comprise a range of $0.025 < z < 0.1$. Table 1 shows a breakdown of the SNe Ia after quality cuts and light-curve fitting. A more thorough review of this selection is found in Möller et al. (2024); Vincenzi et al. (2024). Of note, we do not include bias corrections on the SNIa distance modulus, as we are aiming to

Table 1. SNe and quality cuts.

Cut	Total SNe
SALT3 fit converged and $z > 0.025$	3621
$\|x_1\| < 3$ & $\|c\| < 0.3$	2687
$z < 0.7$	2453
$\sigma_{x_1} < 1$, $\sigma_{t_{\rm peak}} < 2$	2155
FITPROB> 0.001	2056
Host spec-z	1775
$P_{\rm Ia} > 0.5$	1650
Final	**1650**

understand the underlying astrophysical relationships. Further, we follow Kelsey et al. (2022) and place a redshift cut-off $z < 0.7$ on our sample to mitigate potential Malmquist bias in the DES sample.

The host galaxy masses were fit with PEGASE.2 code using a Kroupa (2001) initial mass function. The methodology and star formation history are given in Smith et al. (2020), but in short, the star formation history SED is initialized with a metallicity of 0.004. This metallicity evolves at 102 time-steps from 0 to 14 Gyr, and seven foreground dust screens ranging from 0 to 0.3 mag were applied. We do not modify the DES5YR data, but instead take the fitted parameters directly from the data release.

3 ANALYSIS METHODS

The framework for the simulations presented in this paper has been developed primarily around the SNANA simulation software (Kessler et al. 2009, 2019), with the host galaxy forward model and parameter inference supplied by Wiseman et al. (2022, 2023) and Popovic et al. (2021, 2023b), respectively. We briefly outline each of the procedures below.

3.1 Simulations

We use simulations to test our models; these simulations are generated with SNANA. SNANA broadly works in three steps: fluxes generated from a source model, addition of noise, and detection based on a characterization of survey construction. The simulation output is a set of light curves that are otherwise indistinguishable from the data. From there, the simulations and real data are fitted and treated equivalently.

Our base source model is the newest version of the Spectral Adaptive Light-curve Template (SALT3; Kenworthy et al. 2021) model, an update from SALT2 Guy et al. (2007). SALT3 models the flux of an SN Ia as

$$F(\mathrm{SN}, \mathrm{p}, \lambda) = x_0 \times [M_0(p, \lambda) + x_1 M_1(p, \lambda) + \cdots] \times \exp[cCL(\lambda)], \quad (1)$$

where x_0 is the amplitude of the light curve, x_1 is the fitted light-curve stretch, and c is the SN Ia colour parameter, similar to a $(B - V)$ apparent colour. The M_0, M_1, and $CL(\lambda)$ parameters are determined for the trained model and therefore fixed in this analysis; each SN Ia has a fitted x_0, c, and x_1.

Distances are inferred from SALT3 via the Tripp estimator (Tripp 1998). The distance modulus is given as

$$\mu = m_B + \alpha_{\rm SALT} x_1 - \beta_{\rm SALT} c - M_0, \quad (2)$$

where $m_B = -2.5\log_{10}(x_0)$ and c and x_1 are defined above. The $\alpha_{\rm SALT}$ and $\beta_{\rm SALT}$ are sample-dependent nuisance parameters, following Kenworthy et al. (2021). M_0 is the absolute magnitude in the B-band of an SN Ia with $c = x_1 = 0$. We fit for $\alpha_{\rm SALT}$, $\beta_{\rm SALT}$, M_0 simultaneously for the whole sample when testing each of our models.

3.2 Review of treatment of dust in simulations of SN Ia populations

The aim of this paper is to test the efficacy of dust models therefore here we will briefly review the dust model methodology introduced in Brout & Scolnic (2021) and updated in Popovic et al. (2023b).

Dust models for SNe Ia attribute the distribution of SN Ia colours to an intrinsic, dust-free colour component $c_{\rm int}$ that is reddened by a dust component, following Mandel et al. (2017); Brout & Scolnic (2021). The observed SN Ia colour (c in equation 2) is then modelled as

$$c = c_{\rm int} + E_{\rm dust} + \epsilon_{\rm noise}, \quad (3)$$

where $E_{\rm dust}$ is the dust component and where $\epsilon_{\rm noise}$ is measurement noise not accounted for by a dust model.

The component $E_{\rm dust}$ from equation (3) is interpreted as $E(B - V)$, such that the $V-$band extinction is given by

$$A_V = R_V \times E_{\rm dust}, \quad (4)$$

where R_V is total-to-selective extinction ratio and $E_{\rm dust} = E(B - V)$. The change in observed brightness due to colour, i.e. what is fit as $\beta_{\rm SALT} c$ (from equation 2) can be decomposed into

$$\Delta m_B = \beta_{\rm SN} c_{\rm int} + (R_V + 1) E_{\rm dust} + \epsilon_{\rm noise}. \quad (5)$$

where $\beta_{\rm SN}$ is the intrinsic colour-luminosity relationship, and extinction acts as $R_B = R_V + 1$ in the B-band.

Further review can be found in Brout & Scolnic (2021) and Popovic et al. (2023b).

Of note is that the DES sample includes contamination from non-Ia SNe that may present as degenerate with the effects of reddening and dimming due to dust. Vincenzi et al. (2021) investigates the presence of non-Ia contamination on observed SN Ia properties, and in particular, their fig. 4 shows that with the use of the SuperNNova classifier and a Chauvenet's criteria cut, the expected contamination percentage should be around 2–3 per cent in the $c > 0$ region of SN Ia colour, and consistent with 0 per cent in the range of Hubble Residuals that we investigate. Furthermore, Popovic et al. (2023a) shows that changing the $P_{\rm Ia}$ cut from 0.5 to 0.9 causes a $<1\sigma$ change in the resulting χ^2; demonstrating the efficiacy of the $P_{\rm Ia}$ cut instituted here.

3.3 Host galaxies

Host galaxies are simulated using the physically-motivated empirical model of Wiseman et al. (2022) using the updated prescription of Wiseman et al. (2023). A full description of the simulations can be found in those works. Briefly, seed galaxies evolve following empirical relations that govern their build up of stellar mass (i.e. star-formation history) following the method of Childress, Wolf & Zahid (2014). SNe are associated with galaxies following a probability distribution governed by realistic rates of SNe, themselves driven by the convolution of the SFH of each galaxy and the delay-time distribution of SNe. SNe are designated 'young' (from stellar populations with ages <1 Gyr) or 'old' ($t > 1$ Gyr). The relative number of young and old SNe matches observations well, assuming that SN stretch is driven by this age distribution (Nicolas et al. 2020; Wiseman et al. 2022).

Table 2. A summary of the simulation inputs for the models tested in this paper. In the case that two distributions are provided, the low-mass distribution is listed first, followed by the high-mass distribution.

Model	$E(B-V)$	R_V	$c_{\rm int}$	$\beta_{\rm SN}$
Vincenzi et al. (2024)	exp(0.11), exp(0.13)	$\mathcal{N}(1.71, 0.82), \mathcal{N}(3.17, 1.23)$	$\mathcal{N}(-0.07, 0.053)$	$\mathcal{N}(2.1, 0.22)$
Linear	Table 3	$R_V = -0.41 \times M_* + 8.40 + \mathcal{N}(0.5)$	$\mathcal{N}(-0.074, 0.055)$	$\mathcal{N}(2.1, 0.22)$
Logistic	Binned in mass (Linear)	$\mathrm{expit}(L = 1.5, k = 2, M_*) + 2 + \mathcal{N}(0, 0.5)$	$\mathcal{N}(-0.074, 0.055)$	$\mathcal{N}(2.1, 0.22)$
S18	Binned in mass (Linear)	fig. 3 of S18	$\mathcal{N}(-0.074, 0.055)$	$\mathcal{N}(2.1, 0.22)$

Table 3. Summary of the τ values as a function of host galaxy stellar mass from Linear.

Stellar mass	τ
7.5	0.125
8.0	0.032
8.5	0.093
9.0	0.135
9.5	0.155
10.0	0.155
10.5	0.133
11.0	0.188
11.5	0.113

Here, we use the Wiseman et al. (2022) distribution and relation of x_1 and its relationship to the host galaxy star formation history. This is the only SN Ia parameter that is directly correlated with the host galaxies; m_B is not correlated, and the same intrinsic Gaussian distribution of $c_{\rm int}$ values is used for all supernovae, with $E(B-V)$ and R_V values changing as a function of the host properties.

4 HOST GALAXY DUST RELATIONSHIPS

Here, we outline the models that we test in this paper, which are broadly split into two families. With the exception of the S18 model, our models of dust extinction are derived from empirical measurements of SNe Ia light curves, and are likely tracers of the line-of-sight *extinction*; this is in contrast to S18, which provides measurements of the *attenuation* of light due to dust.

In each of the following sections, we lay out different models for testing distributions of R_V and $E(B-V)$ and how they relate to host galaxy properties. The four remaining 'dust-free' parameters that characterize the intrinsic properties of the SN Ia scatter model are the mean and standard deviation for the Gaussian distribution of $c_{\rm int}$ and $\beta_{\rm SN}$. Here, we make note that $\beta_{\rm SN}$ is not the same as the one from the $\beta_{\rm SALT}$ in equation (2): $\beta_{\rm SALT}$ from equation (2) is fit from the data, and is a convolution of $\beta_{\rm SN}$ and other dust effects.

We fix the intrinsic colour and intrinsic $\beta_{\rm SN}$ by using a single population that follows a Gaussian distribution for each; we use the values from Vincenzi et al. (2024): $\mu_c = -0.7$, $\sigma_c = 0.053$; $\mu_\beta = 2.07$, $\sigma_\beta = 0.22$.

4.1 Baseline model: DES

Our baseline simulation model uses the model parameters from the DES 5-year cosmological results (Vincenzi et al. 2024). These parameters, which describe distributions for $c_{\rm int}$, R_V, $E_{\rm dust}$, and $\beta_{\rm SN}$, are simultaneously fit using the `Dust2Dust` program from Popovic et al. (2023b), providing two populations of R_V ($\mu_{\mathrm{RV}_{\rm high}} = 1.66$, $\mu_{\mathrm{RV+low}} = 3.25$) that are split on the host galaxy stellar mass, specifically at $\log(M_*) = 10$. The data used for the `Dust2Dust` training process have a cut on the photometric classification probability that the light curve is a SN Ia, $P_{\rm Ia} > 0.5$ applied. However, the representation of this data in Vincenzi et al. (2024), fig. 5, does not include the $P_{\rm Ia}$ cut in its visualization, and uses the best-fit DES5YR cosmology as its reference. Here, for consistency, we have re-instituted the $P_{\rm Ia} > 0.5$ cut, as we wish to similarly avoid non-Ia contamination in the testing of our model parameters. We show the models in Fig. 1.

4.2 Linear R_V and $E(B-V)$ (Linear)

Popovic et al. 2024 (hereafter the Linear model) compiles a volume-limited sample of SNe Ia from DES, the Zwicky Transient Facility, the Sloan Digital Sky Survey, and Pan-STARRS photometric SN Ia samples. To this collected sample, they fit a Gaussian intrinsic colour and an exponential $E(B-V)$ dust tail, described by the parameter τ, to their SN Ia colour distribution as a function of host galaxy mass and redshift. This provides a statistical probability of the mean reddening, τ, given a redshift and host galaxy mass for each supernova. Here, we use their exponential reddening values (τ).

Furthermore, the Linear model similarly splits the data into uniform bins of host galaxy stellar mass, starting at $\log(M_*) = 7.5$ to $\log(M_*) = 11.5$, in steps of $\log(M_*) = 0.5$. In each of these bins, a $\beta_{\rm SALT2}$ is fit to the data, providing a measurement of a mass-varying $\beta_{\rm SALT2}$. We use these $\beta_{\rm SALT2}$ fits to describe the relationship of R_V to host galaxy mass, assuming $\beta_{\rm SALT} = R_V + 1$ to correspond to the B-band.

The Linear model therefore draws an $E(B-V)$ reddening value depending on the exponential distribution defined by the τ value in each mass bin, given in Table 3. The R_V values are taken from the linear equation in Table 2, compared to the two-Gaussian R_V and two-exponential distributions of the fiducial DES model.

This approach of using the $\beta_{\rm SALT}$, which is a convolution of $\beta_{\rm SN}$ and R_V, to infer an R_V distribution does run the risk of double counting the colour-luminosity relationship. However, with our assumption of a single $\beta_{\rm SN}$ distribution, equation (5) demonstrates this approach will preserve the likely slope of the R_V-host galaxy stellar mass relationship that we wish to investigate.

4.3 Logistic R_V curve (Logistic)

It is unphysical to assume R_V to be governed by a simple step function, whether with stellar mass or any other continuous host galaxy property. Here, we model the R_V distribution of our sample as a function of host galaxy mass M_* using a logistic function:

$$R_V = \frac{1.5}{1 + \mathrm{e}^{2(\log(M_*)-10)}} + 2, \quad (6)$$

where $L = 1.5$ and $k = 2$.

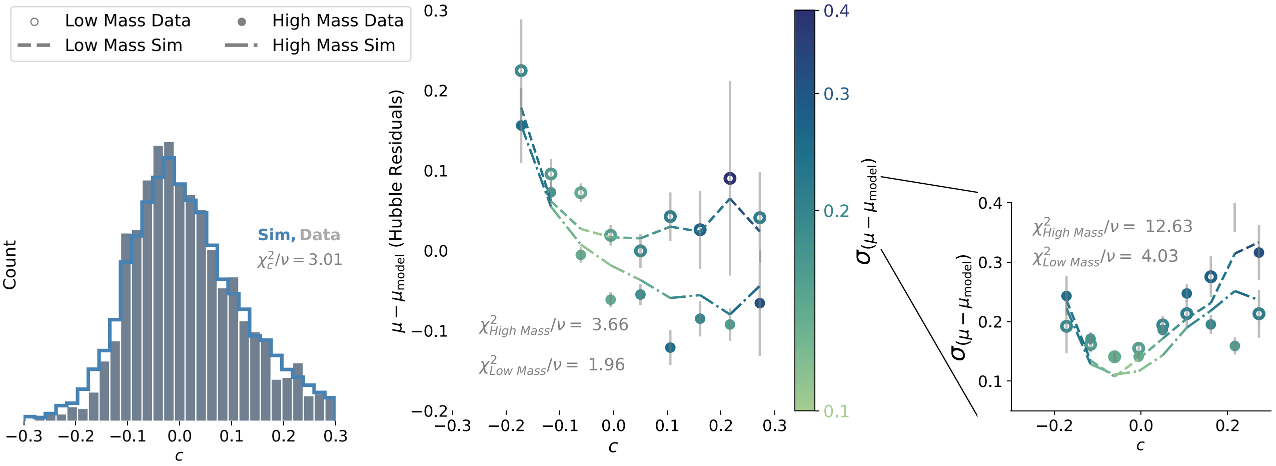

Figure 1. Plots of the metrics used to measure goodness of fit. Histogram of c, $\mu_{\rm res}$ as a function of c, and $\sigma_{\mu{\rm res}}$ as a function of c are shown left to right. For the c versus $\mu_{\rm res}$ and c versus $\sigma_{\mu{\rm res}}$ plots, we split on the host galaxy mass M_*; high-mass and low-mass data are represented in closed and open circles, respectively, and simulations are shown in dash–dotted and dashed lines for high- and low-mass simulations. The c versus $\mu_{\rm res}$ plot is colour coded by the Hubble scatter in each colour bin, this is elucidated in the rightmost figure. Here, we present the DES5YR data and their nominal simulation.

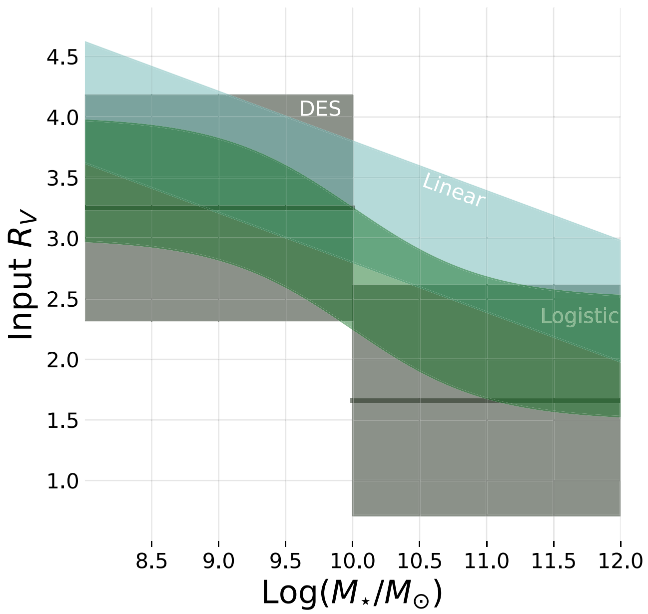

Figure 2. An illustration of the input R_V values for our SNIa inferred models. The fiducial DES model in dark grey assumes two Gaussian distributions split on $\log(M_*/\mathrm{M}_\odot) = 10$, as opposed to the continuously-varying Linear (turqoise) and Logistic (dark green) models.

We choose the logistic curve as a smoothly varying R_V that spans the range of $R_V = 3.5$ in the extreme low-host galaxy mass ($\log(M_*) < 8$) to 2.0 in the extreme high-host galaxy mass ($\log(M_*) > 12$). We add a Gaussian error with $\sigma = 0.5$ to the R_V values. Our choice of an R_V threshold of 2 is motivated to avoid the $R_V = 1.2$ Rayleigh scattering threshold, while maintaining a smooth function. The $L = 1.5$ and $k = 2$ values were chosen to mimic the $\Delta R_V = 1.5$ range and transition from other dust models, and are shown in Fig. 2. We use the same τ values from Linear to describe the exponential reddening for this and subsequent tests.

4.4 Salim et al. 2018

We obtain the specific star formation rate/host galaxy mass/R_V contours from S18 and include the R_V information in our host library. S18 performs an SED fit on 230 000 galaxies using photometry from *GALEX*, *SDSS*, and *WISE*. This SED fitting across multiple bands allows them to constrain star formation and R_V across a range of galaxies from quiescent to star forming systems. We specifically use the data from the 'Slope (all galaxies)' contour in fig. 3 in S18. During the simulation process, each SN Ia is generated in a galaxy with a defined SFR and stellar mass. An R_V value is then randomly drawn from the S18 contours in the appropriate region of SFR and stellar mass space.

We use the $E(B - V)$ distribution from Linear for this test.

4.5 Logistic and S18 with Intrinsic Step (+Step)

Here, we repeat the previous two models in Sections 4.3 (Logistic) and 4.4 (S18), but with the addition of a luminosity step as a function of SN Ia age. We place our 'age step' at $\log_{10}(\mathrm{SN\ age}/1\ \mathrm{Gyr}) = 1$, following Wiseman et al. (2022) and Wiseman et al. (in prep.).

Additionally, we test the effects of an increasing age step on our Logistic R_V model, with particular focus on how this luminosity step affects our Hubble Residual scatter. We increase the age step in steps of 0.08 mag from 0 to 0.32 mag.

Works such as Rigault et al. (2018), Briday et al. (2022), Kelsey et al. (2022), and Wiseman et al. (2022, 2023) suggest that a luminosity step may be driven by properties other than the host galaxy stellar mass; we adopt this assumption in order to test not only the recovery of the mass step, but also the hypothesis that there may be a luminosity step that is driven by processes for which the host galaxy stellar mass acts as a biased tracer. Other works, such as González-Gaitán et al. (2021), suggest that the luminosity step may arise from two separate populations of intrinsic colour. This model is incompatible with the baseline simulations from DES and would require a simultaneous fit of the two intrinsic populations and the dust distributions, which will be left to another paper.

4.6 R_V Variation

Here, we investigate the impact of increasing scatter in the R_V distribution on our dust models. We again use the Logistic R_V curve from Section 4.3, but replace the Gaussian scatter with increasing values. The first test begins with 0 scatter in the R_V distribution, and we increase the σ_{R_V} in each test by steps of 0.2, up to a maximum value of 0.8.

5 RESULTS

To determine the efficacy of our models, we follow the criteria and method provided by Popovic et al. (2023b). While detailed further in that paper, we briefly detail the three criteria here, whereby the χ^2 are computed between simulations and data:

χ^2_c: Comparison of the SN Ia c distribution, with Poisson errors:

$$\chi^2_c = \sum_i \left(N^{\rm data}_{c_i} - N^{\rm sim}_{c_i}\right)^2 / {\rm e}^2_{ni}. \tag{7}$$

$\chi^2_{\mu\rm res}$: The c versus Hubble Residual $\mu_{\rm res}$ ($\mu_{\rm res} = \mu - \mu_{\rm model}$) curves, split on high- and low mass (split at $10M_*$), with $e_{\mu_{\rm res}} = \sigma/\sqrt{N}$, where σ is the standard deviation of the Hubble Residuals.

$$\chi^2_{\mu_{\rm res}} = \sum_i \left(\mu^{\rm data}_{\rm res_i} - \mu^{\rm sim}_{\rm res_i}\right)^2 / {\rm e}^2_{\mu_{\rm res_i}}. \tag{8}$$

$\chi^2_{\rm RMS}$: The scatter in Hubble Residuals as a function of c, split on high and low mass (split at $10M_*$). We measure the scatter with the median absolute deviation, and $e_{\rm RMS} = \sigma/\sqrt{2N}$.

$$\chi^2_{\sigma_{\rm r}} = \sum_i \left(\sigma^{\rm data}_{\rm r_i} - \sigma^{\rm sim}_{\rm r_i}\right)^2 / {\rm e}^2_{\sigma_{\rm r}i}. \tag{9}$$

Of note, we use a finer colour binning than Popovic et al. (2023b) – ten uniform colour bins, ranging from $c = -0.2$ to 0.3. This same colour binning is used in all three of our metrics. The baseline model that we use, from Vincenzi et al. (2024), is presented in Fig. 1 alongside our three metrics.

The χ^2_ν values for all of our tested models are given in Table 4, and we go over in further depth here. From here, we report our reduced χ^2/ν values without the ν denominator for visual clarity. Figs A1 through A6 in the appendix show the results for each model tested.

5.1 Baseline

Despite some changes in the data between this analysis and Vincenzi et al. (2024), notably $P_{\rm Ia} > 0.5$ and $z < 0.7$ cuts, we find good agreement between our baseline model from DES and the data.

5.2 Linear R_V (Linear)

We find relatively good agreement between the Linear model simulations and data. The overall performance of the Linear model is comparable to the baseline DES, though neither models the high-mass Hubble Residual scatter well.

5.3 Logistic R_V curve (logistic)

We find that the logistic R_V performs well in replicating the data. The logistic curve improves on both the $\mu_{\rm res}$and Hubble Residual scatter curves. Logistic R_V does not replicate $\mu_{\rm res}$ versus c as well as the DES5YR baseline in the red $c > 0$ regime but performs better in the blue $c < 0$ where it reproduces roughly half of the mass step.

5.4 Salim et al. 2018

Overall, S18 performs comparably to our base model. However, S18 performs worse in modelling $\mu_{\rm res}$. Current dust models attribute the mass step to differences in the mean of the R_V distribution when split on mass: S18 does not produce a large difference: $\Delta R_V = \sim 0.5$. Therefore, S18 does not well reproduce the mass step, unlike other models.

5.5 Logistic and S18 with Intrinsic Step (+Step)

We find that the addition of an intrinsic luminosity step that is dependent on the age of the SN Ia presents a small but overall improvement to our models. Table 6 shows the Hubble Residual scatter $\chi^2_{\nu,\rm RMS}$ and total χ^2_ν for our tested magnitudes of the age step. In our coarse search, we find that a step size $\gamma = 0.16$ returns the best χ^2_ν value, and that the majority of this improvement in modelling the χ^2_ν comes from improved matches in the Hubble Residual scatter. We emphasize that we have modelled this additional step as an intrinsic difference in M_0 but it could equally well come from two intrinsic colour populations, or a combination of both. The source of this step is not addressed further in this work.

5.6 R_V Variation

We test the impact of increased scatter of R_V values on our data by adding increasing amounts of Gaussian scatter onto the Logistical R_V function. Table 5 shows the impact of the σR_V choice on our logistic R_V model. There is not a strong correlation between σR_V and the total χ^2_ν; higher σR_V such as $\sigma R_V \geq 0.8$, are ruled out by the increased χ^2_ν. In contrast to the γ, the Hubble Residual scatter $\chi^2_{\nu,\rm RMS}$ is largely static below $\sigma R_V < 0.5$. We find that our best-fit $\sigma R_V = 0.5$, though again stress that this is still a coarse fit.

5.7 Recovery of $\beta_{\rm SALT2}$

Fig. 3 shows that the DES data display the same relationship between $\beta_{\rm SALT}$ and host stellar mass as Linear: beta decreases with increasing host stellar mass. The recovered Tripp β for each of our models is well-matched to the data. In contrast, none of our models are able to entirely recover the range of the observed β versus host galaxy mass relationship seen in the data, though each model is well-able to replicate the β value when marginalizing over the host galaxy stellar mass.

6 DISCUSSION AND CONCLUSIONS

In this paper, we have reviewed a number of different methods to model dust distributions and properties for use in standardization of SNe Ia and evaluated their efficacy. We have included an age-dependent luminosity step that is independent of the dust of the host galaxy to test alongside these methods, and compared them to dust-only methods. Here, we will discuss our results.

6.1 SN Ia Hubble Residual scatter

The single largest χ^2_ν contribution across all models we have tested is the high-mass Hubble Residual scatter, $\sigma_{\mu\rm RMS}$. We do see slight improvements to the high-mass $\sigma_{\mu\rm RMS}\,\chi^2/\nu$ values when including an age-based luminosity step, up to a χ^2/ν reduction of $\sim$2 in the case of $\gamma = 0.16$. Higher values are ruled out by an increasing $\chi^2_{\nu,\rm RMS}$, putting an upper limit on this value.

Table 4. χ^2/ν values for the dust models presented in this work, where $\nu = 27$.

Model	Vincenzi et al. (2024) (DES, base)	Linear	Logistic R_V (Logistic)	S18	Logistic+Step	S18+Step
$\chi^2_{\nu,c}$	3.0	2.9	2.5	2.5	2.5	2.5
High mass $\chi^2_{\nu,\mu\mathrm{res}}$	3.7	4.2	3.3	6.4	2.7	5.7
Low mass $\chi^2_{\nu,\mu\mathrm{res}}$	2.0	3.7	1.5	8.6	1.0	6.3
High mass $\chi^2_{\nu,\mathrm{RMS}}$	12.6	14	12	13	11	12
Low mass $\chi^2_{\nu,\mathrm{RMS}}$	4.0	1.0	3.0	5.0	3.0	5.0
Total χ^2_ν	**25.3**	**25.8**	**22.3**	**35.5**	**20.2**	**31.5**

Table 5. χ^2_ν results for increasing values of σR_V, tested with the Logistic R_V distribution.

Model	$\chi^2_{\nu,\mathrm{RMS}}$	Total χ^2_ν
$\sigma R_V = 0.5$ (reference)	15.3	**22.7**
$\sigma R_V = 0$	19.6	**27.1**
$\sigma R_V = 0.2$	19.2	**27.0**
$\sigma R_V = 0.4$	19.8	**27.3**
$\sigma R_V = 0.6$	16.7	**25**
$\sigma R_V = 0.8$	22.3	**30.7**

Table 6. χ^2_ν results for increasing values of γ, tested with the Logistic R_V distribution.

Model	$\chi^2_{\nu,\mathrm{RMS}}$	Total χ^2_ν
$\gamma = 0$ (reference)	15.3	**22.7**
$\gamma = 0.08$	12.6	**18.9**
$\gamma = 0.16$	10.5	**16.4**
$\gamma = 0.24$	25.4	**33.6**
$\gamma = 0.32$	76.8	**88.8**

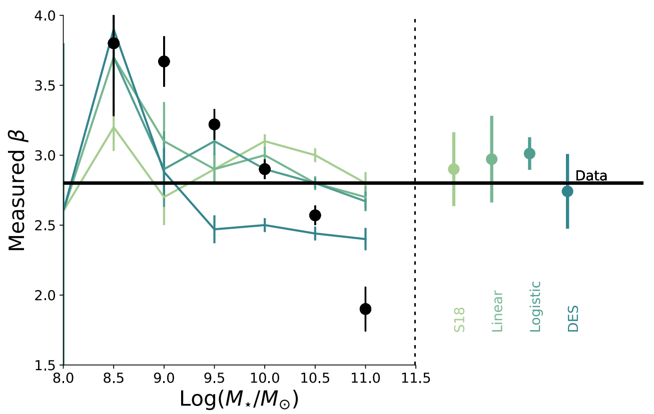

Figure 3. The β versus host galaxy mass relationship for the DES data (black points) and each of our tested models (coloured lines). On the right, the conventional Tripp β, which is marginalized over mass, is presented for each model.

The σR_V, variation, on the other hand, does not present a strong constraint on our models. First, this would indicate that variations in R_V are not responsible for the observed Hubble residual scatter, as we would expect to see improved fits to the Hubble residual scatter with a greater R_V variation. Instead, we find that any $\sigma R_V \leq 0.4$ is equally supported by the data, likely a sign of a detection threshold in the data that we cannot detect a variation in σR_V below 0.4.

Overall, all of our tested models noticeably underestimate the scatter seen in SNe Ia. The addition of a colour/mass-independent scatter floor of $\sim$0.02 improves our $\sigma_{\mu\mathrm{RMS}}\chi^2_\nu$ values by a factor of approximately two. This can be compensated by an age step, indicating that dust is not the only element at play in the observed SN Ia scatter.

6.2 SN Ia dust distributions

The logistic R_V distribution provides an improved model for dust to be the sole contributor to SN Ia scatter and the mass step. None the less, the model is unable to replicate the necessary level of Hubble Residual scatter, and unable to recreate the mass step.

Approaching from the alternative direction of galaxy observations, we find that SNe Ia with host galaxy dust properties drawn from the global galaxy population do not well match either of our Hubble Residual or scatter metrics, failing to recreate the mass step. This is because after mapping the SN Ia host galaxy stellar mass function onto the S18 galaxy R_V values, there is an *increase* in R_V with the host galaxy stellar mass, contrary to the predictions of contemporary dust models (including our Logistic function), which require *lower* R_V in more massive hosts.

The S18 results indicate that sSFR, rather than stellar mass, does show a change of R_V in the sense required by the SN Ia distances: a galaxy at fixed stellar mass will have a lower R_V if it has a lower sSFR. Nevertheless, this trend works against the trend of increasing R_V with stellar mass in the star-forming galaxies, such that the low-mass star-forming galaxies and high-mass passive galaxies have comparable R_V values. We illustrate this in Fig. 4, which shows the R_V verus stellar mass relationship for simulated SNe Ia, colour coded by the log(sSFR) value of the galaxy. Even excluding all high-mass star-forming galaxies, the largest ΔR_V between low- and high-mass galaxies is $\sim$0.3, less than the values needed to recreate the mass step with R_V alone: $\Delta R_V = \sim 1$. The presence of star-forming galaxies will serve only to increase the median R_V value in high-mass galaxies.

6.3 Dark dust

Instead of an intrinsic luminosity difference causing the unexplained step in SNe of all colours, an offset could be introduced by so-called 'dark dust'. Dark dust (e.g. Siebenmorgen, Krügel & Chini 1999) is not selective in its extinction, such that all wavelengths are equally extinguished. If there were systematically more dark dust along sight lines to SNe Ia in young star-forming environments than those in older passive environments, then those SNe would be systematically fainter regardless of their colour. There is tentative evidence for such a trend based on the emission from cold dust grains in passive galaxies (Krugel et al. 1998; Siebenmorgen et al. 1999).

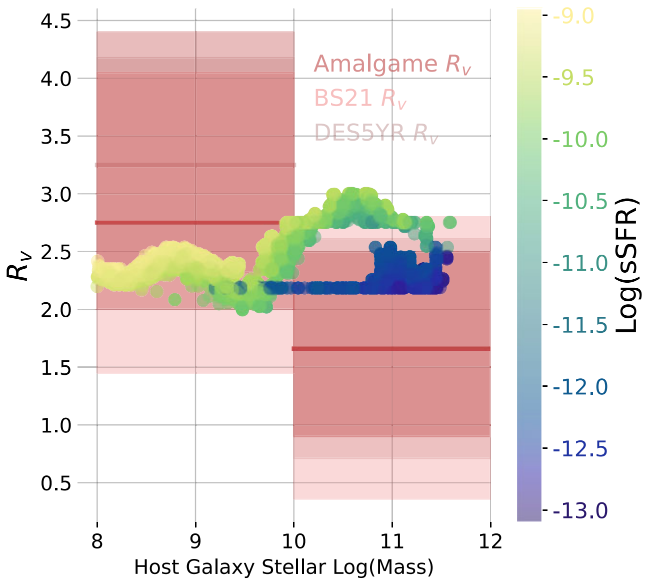

Figure 4. The simulated R_V versus host galaxy stellar mass relationship colour coded by log(sSFR), based on the galaxy data from S18. The trend of increasing R_V with host galaxy stellar mass is opposite to that predicted by contemporary SN Ia dust-based scatter models, which are shown in shades of red. The high-mass R_V values for the contemporary SN Ia dust models overlap strongly.

6.4 Multiple intrinsic populations

Instead of, or complementary to, a variation in the *extrinsic* effects of dust extinction, another method to explain and alleviate the host galaxy step is by assuming there are multiple populations of *intrinsic* SN Ia parameters which correspond to one or more progenitor scenario and/or explosion mechanism. Our Logistic + Intrinsic Step model is a simple such example. Evidence for multiple populations already exists in the SN stretch parameter (Rigault et al. 2018; Wiseman et al. 2022; Ginolin et al. 2024). Wojtak, Hjorth & Hjortlund (2023) find evidence for two populations over both SN stretch and SN colour: a population of faster, redder SNe and a population of slower, bluer SNe. The distribution of these populations across host galaxies is not homogeneous (as expected given the well established stretch–host correlation (e.g. Mannucci, Della Valle & Panagia 2006; Sullivan et al. 2006; Rigault et al. 2013; Ginolin et al. 2024) and Wojtak et al. (2023) suggest that a significant fraction of the host mass step can be explained if these two populations have different mean absolute magnitudes, although it is unlikely to be able to explain the diverging Hubble residuals in redder SNe that motivates the use of the R_V parameter in this work. The Wojtak et al. (2023) model is trained on a different data set, and to apply the model to DES-SN5YR data would require it to be retrained on the DES data which is a full analysis in its own right and is deferred to future work.

6.5 Conclusions

We conclude that if a varying R_V is responsible for the SN Ia mass step and its evolution with SN colour, then the extinction along SN Ia lines of sight, and its relationship with the host galaxy properties, is not well reproduced by the corresponding global attenuation of SN Ia host galaxies. There are four possible explanations for this behaviour:

(i) the attenuation measured from integrated galaxy observations, and how it relates to global galaxy properties, is not representative of how line-of-sight extinction varies with these properties, and/or

(ii) SNe Ia are preferentially observed along lines of sight at the extreme ends of dust distributions, and/or

(iii) Galaxies contain significant quantities of dark dust, and there is systematically more in low-mass, star-forming environments, and/or

(iv) There is an intrinsic brightness difference in SNe Ia that evolves with SN colour but is not caused by dust, such as two populations of M_0 or $c_{\rm int}$.

The inability of our dust-only models from the literature to recreate the mass step appears to match with near-infrared measurements of SNe Ia, particularly Thorp et al. (2021) and Ward et al. (2023), both analyses of SNe Ia with the BayeSN light curve fitter. These studies do not find a significant ΔR_V between high- and low-mass galaxies.

We conclude that a portion of the observed mass step is likely caused by an intrinsic brightness difference closely related to the age of the SN progenitor and its local environment, and that an especially large $\Delta R_V(>1)$ is not supported by galactic R_V distributions. This may be due to SNe Ia preferentially selecting the extremes of an R_V distribution, but it is more likely that the method of measuring R_V and $E(B-V)$ for SNe and galaxies are incompatible. Measuring the dust of a supernova involves a single line of sight and can be described as extinction, whereas a non-point source measurement across a galaxy requires accounting for attenuation and scattering; this is described further in Chevallard et al. (2013), Narayanan et al. (2018), and Duarte et al. (2022).

The discrepancy between the SN Ia extinction and galactic attenuation presents a new difficulty for using the host galaxy properties of an SN Ia to standardize its distance, and further work must be done to determine a way to connect the host galaxy dust properties to the dust that is along the line of sight to the supernova. It appears that these initial attempts to directly provide a one-to-one correlation between the properties of the host galaxy and its supernova will need continuing research.

The introduction of an age step partially ameliorates the need of an otherwise quite large ΔR_V between high- and low-mass galaxies, but this benefit primarily occurs in our modelling of the Hubble Residual scatter, rather than the mass step itself. That the size of the age step does not make a large impact on the mass step is explained by Wiseman et al. (in prep.), but points to further work on disentangling different tracers of anomalous luminosity offsets.

In the shorter term, incorporating dust into SN Ia standardization has provided benefits beyond modelling the mass step, being able to better recreate the observed scatter in SN Ia data, and engendering a more realistic understanding than post-hoc grey scatter additions (Brout & Scolnic 2021; Popovic et al. 2021, 2023a; Brout et al. 2022). We provide an improvement to the R_V step used in previous literature (e.g. Brout & Scolnic (2021); Wiseman et al. (2022); Popovic et al. (2023b)) via the use of a smoothly varying logistic function that performs better than a linearly-varying R_V distribution. Here, we have not rigorously optimized the logistic R_V nor the age step size; such work ought to be incorporated into pipelines such as UNITY (Rubin et al. 2015) or Dust2Dust (Popovic et al. 2023b).

ACKNOWLEDGEMENTS

All authors have read and contributed to the drafting of the manuscript. BP devised the analysis, ran the simulations and drafted the majority of the manuscript. PW, MSu, and MSm provided scientific support throughout the analysis and writing. SG-G and DS internally reviewed the work and provided extensive feedback. JD, LG, LK, RK, CL, JL, MT, and MV provided comments on the analysis and interpretation. The remaining authors have made contributions to this paper that include, but are not limited to, the construction of DECam and other aspects of collecting the data; data processing and calibration; developing broadly used methods, codes, and simulations; running the pipelines and validation tests; and promoting the science analysis.

PW acknowledges support from the Science and Technology Facilities Council (STFC) grant ST/R000506/1. AM is supported by the ARC Discovery Early Career Researcher Award (DECRA) project number DE230100055

Funding for the DES Projects has been provided by the U.S. Department of Energy, the U.S. National Science Foundation, the Ministry of Science and Education of Spain, the Science and Technology Facilities Council of the United Kingdom, the Higher Education Funding Council for England, the National Center for Supercomputing Applications at the University of Illinois at Urbana-Champaign, the Kavli Institute of Cosmological Physics at the University of Chicago, the Center for Cosmology and Astro-Particle Physics at the Ohio State University, the Mitchell Institute for Fundamental Physics and Astronomy at Texas A&M University, Financiadora de Estudos e Projetos, Fundação Carlos Chagas Filho de Amparo à Pesquisa do Estado do Rio de Janeiro, Conselho Nacional de Desenvolvimento Científico e Tecnológico and the Ministério da Ciência, Tecnologia e Inovação, the Deutsche Forschungsgemeinschaft and the Collaborating Institutions in the Dark Energy Survey.

The Collaborating Institutions are Argonne National Laboratory, the University of California at Santa Cruz, the University of Cambridge, Centro de Investigaciones Energéticas, Medioambientales y Tecnológicas-Madrid, the University of Chicago, University College London, the DES-Brazil Consortium, the University of Edinburgh, the Eidgenössische Technische Hochschule (ETH) Zürich, Fermi National Accelerator Laboratory, the University of Illinois at Urbana-Champaign, the Institut de Ciències de l'Espai (IEEC/CSIC), the Institut de Física d'Altes Energies, Lawrence Berkeley National Laboratory, the Ludwig-Maximilians Universität München and the associated Excellence Cluster Universe, the University of Michigan, NSF NOIRLab, the University of Nottingham, The Ohio State University, the University of Pennsylvania, the University of Portsmouth, SLAC National Accelerator Laboratory, Stanford University, the University of Sussex, Texas A&M University, and the OzDES Membership Consortium.

Based in part on observations at NSF Cerro Tololo Inter-American Observatory at NSF NOIRLab (NOIRLab Prop. ID 2012B-0001; PI: J. Frieman), which is managed by the Association of Universities for Research in Astronomy (AURA) under a cooperative agreement with the National Science Foundation.

The DES data management system is supported by the National Science Foundation under Grant Numbers AST-1138766 and AST-1536171. The DES participants from Spanish institutions are partially supported by MICINN under grants PID2021-123012, PID2021-128989, PID2022-141079, SEV-2016-0588, CEX2020-001058-M, and CEX2020-001007-S, some of which include ERDF funds from the European Union. IFAE is partially funded by the CERCA program of the Generalitat de Catalunya.

We acknowledge support from the Brazilian Instituto Nacional de Ciência e Tecnologia (INCT) do e-Universo (CNPq grant 465376/2014-2).

SGG and JD acknowledge support by FCT for CENTRA through the Project No. UIDB/00099/2020. JD also acknowledges support by FCT under the PhD grant 2023.01333.BD.

This manuscript has been authored by Fermi Research Alliance, LLC under Contract No. DE-AC02-07CH11359 with the U.S. Department of Energy, Office of Science, Office of High Energy Physics.

DATA AVAILABILITY

Data used in this article is publicly available with the DES5YR data release (Sánchez et al. 2024).

REFERENCES

Briday M. et al., 2022, A&A, 657, A22
Brout D., Scolnic D., 2021, ApJ, 909, 26
Brout D. et al., 2022, ApJ, 938, 110
Burns C. R. et al., 2011, AJ, 141, 19
Burns C. R. et al., 2014, ApJ, 789, 32
Chevallard J., Charlot S., Wandelt B., Wild V., 2013, MNRAS, 432, 2061
Childress M. J., Wolf C., Zahid H. J., 2014, MNRAS, 445, 1898
Childress M. J. et al., 2017, MNRAS, 472, 273
Duarte J. et al., 2022, A&A, 680, A56
Flaugher B. et al., 2015, AJ, 150, 150
Foley R. J. et al., 2018, MNRAS, 475, 193
Gao H., Lei W.-H., Zou Y.-C., Wu X.-F., Zhang B., 2013, New A Rev., 57, 141
Ginolin M. et al., 2024, preprint (arXiv:2406.02072)
González-Gaitán S., de Jaeger T., Galbany L., Mourão A., Paulino-Afonso A., Filippenko A. V., 2021, MNRAS, 508, 4656
Grayling M., Thorp S., Mandel K. S., Dhawan S., Uzsoy A. S., Boyd B. M., Hayesn E. E., Ward S. M., 2024, MNRAS, 531, 953
Guy J., Astier P., Nobili S., Regnault N., Pain R., 2005, A&A, 443, 781
Guy J. et al., 2007, A&A, 466, 11
Hicken M., Wood-Vasey W. M., Blondin S., Challis P., Jha S., Kelly P. L., Rest A., Kirshner R. P., 2009, ApJ, 700, 1097
Hicken M. et al., 2012, ApJS, 200, 12
Jha S., Riess A. G., Kirshner R. P., 2007, ApJ, 659, 122
Johansson J. et al., 2021, ApJ, 923, 237
Kelly P. L., Hicken M., Burke D. L., Mandel K. S., Kirshner R. P., 2010, ApJ, 715, 743
Kelsey L. et al., 2022, MNRAS, 527, 8015
Kenworthy W. D. et al., 2021, ApJ, 923, 265
Kessler R. et al., 2009, PASP, 121, 1028
Kessler R. et al., 2019, PASP, 131, 094501
Krisciunas K. et al., 2017, AJ, 154, 211
Kroupa P., 2001, MNRAS, 322, 231
Krugel E., Siebenmorgen R., Zota V., Chini R., 1998, A&A, 331, L9
Lampeitl H. et al., 2010, ApJ, 722, 566
Lidman C. et al., 2020, MNRAS, 496, 19
Mandel K. S., Narayan G., Kirshner R. P., 2011, ApJ, 731, 120
Mandel K. S., Scolnic D. M., Shariff H., Foley R. J., Kirshner R. P., 2017, ApJ, 842, 93
Mannucci F., Della Valle M., Panagia N., 2006, MNRAS, 370, 773
Möller A., de Boissière T., 2020, MNRAS, 491, 4277
Möller A. et al., 2024, MNRAS, 533, 2073

Narayanan D., Conroy C., Davé R., Johnson B. D., Popping G., 2018, ApJ, 869, 70
Nicolas N. et al., 2021, A&A, 649, A74
Perlmutter S. et al., 1999, ApJ, 517, 565
Phillips M. M., 1993, ApJ, 413, L105
Popovic B., Brout D., Kessler R., Scolnic D., Lu L., 2021, ApJ, 913, 49
Popovic B. et al., 2023a, MNRAS, 529, 2100
Popovic B., Brout D., Kessler R., Scolnic D., 2023b, ApJ, 945, 84
Popovic B. et al., 2024, preprint (arXiv:2406.06215)
Riess A. G., Press W. H., Kirshner R. P., 1996, ApJ, 473, 88
Riess A. G. et al., 1998, AJ, 116, 1009
Rigault M. et al., 2013, A&A, 560, A66
Rigault M. et al., 2020, A&A, 644, A176
Rose B. M., Garnavich P. M., Berg M. A., 2019, ApJ, 874, 32
Rubin D. et al., 2015, ApJ, 813, 137
Salim S., Boquien M., Lee J. C., 2018, ApJ, 859, 11
Sánchez B. O. et al., 2024, preprint (arXiv:2406.05046)
Schlafly E. F. et al., 2016, ApJ, 821, 78
Siebenmorgen R., Krügel E., Chini R., 1999, A&A, 351, 495
Smith M. et al., 2020, MNRAS, 494, 4426
Sullivan M. et al., 2006, ApJ, 648, 868
Sullivan M. et al., 2010, MNRAS, 406, 782
Sullivan M. et al., 2011, ApJ, 737, 102
Thorp S., Mandel K. S., Jones D. O., Ward S. M., Narayan G., 2021, MNRAS, 508, 4310
Tripp R., 1998, A&A, 331, 815
Vincenzi M. et al., 2021, MNRAS, 518, 1106
Vincenzi M. et al., 2024, preprint (arXiv:2401.02945)
Ward S. M., Dhawan S., Mandel K. S., Grayling M., Thorp S., 2023, MNRAS, 526, 5715
Wiseman P. et al., 2020, MNRAS, 495, 4040
Wiseman P. et al., 2022, MNRAS, 515, 4587
Wiseman P., Sullivan M., Smith M., Popovic B., 2023, MNRAS, 520, 6214
Wojtak R., Hjorth J., Hjortlund J. O., 2023, MNRAS, 525, 5187
Yuan F. et al., 2015, MNRAS, 452, 3047

APPENDIX A:

We provide additional visualizations of our model criteria for each of the models tested here: Figs A1 through A6.

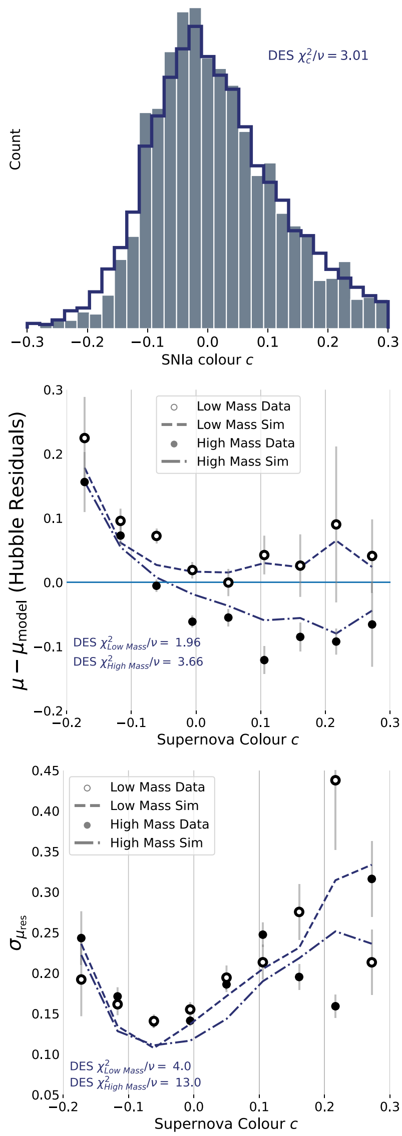

Figure A1. Goodness-of-fit criteria for the baseline DES model. Top panel is the colour distribution, with data in grey bars and simulation in solid histogram. Middle panel is the c versus Hubble Residuals relationship, split on the host galaxy stellar mass. High-mass mass data is presented in filled circle, low-mass data in open circle. High-mass simulations are shown in dashed line, low-mass simulations in dash–dotted line. Bottom panel shows the scatter in the Hubble Residuals, with the same presentation as the middle panel.

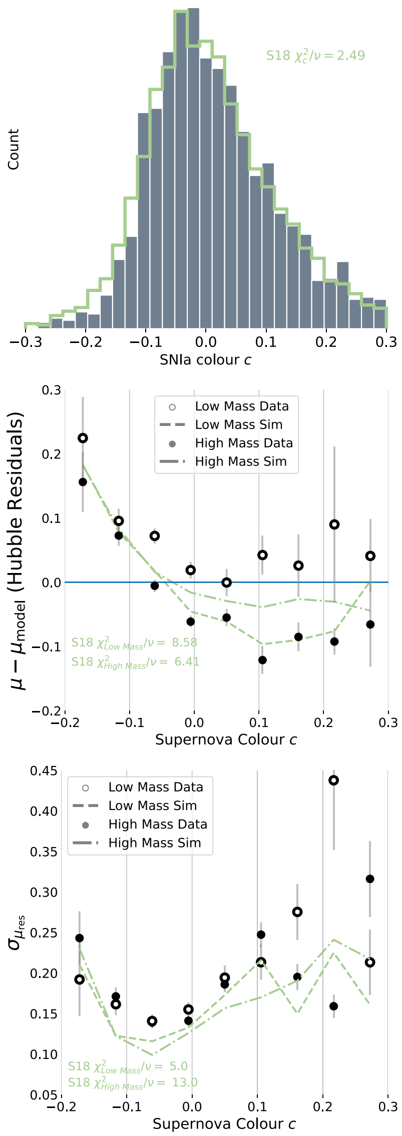

Figure A2. Goodness-of-fit criteria for the S18 model. Top panel is the colour distribution, with data in grey bars and simulation in solid histogram. Middle panel is the c versus Hubble Residuals relationship, split on the host galaxy stellar mass. High-mass data is presented in filled circle, low-mass data in open circle. High-mass simulations are shown in dashed line, low-mass simulations in dash–dotted line. Bottom panel shows the scatter in the Hubble Residuals, with the same presentation as the middle panel.

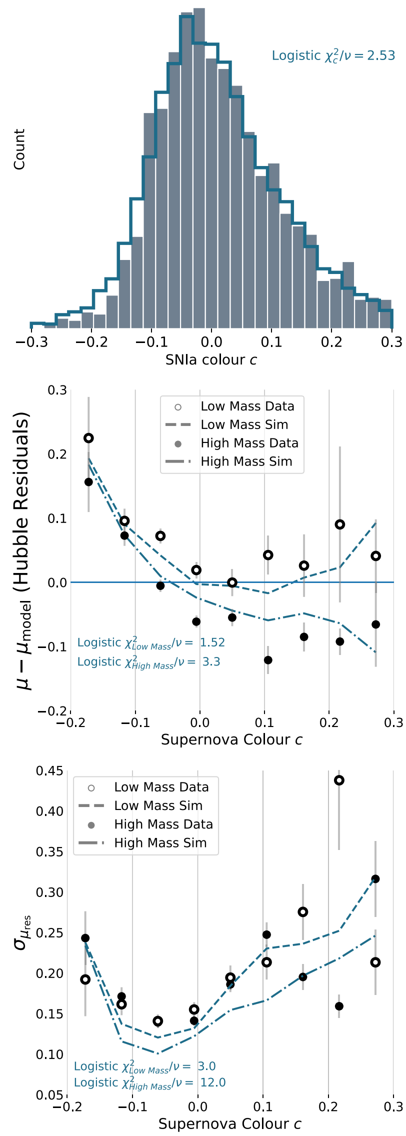

Figure A3. Goodness-of-fit criteria for the Logistic model. Top panel is the colour distribution, with data in grey bars and simulation in solid histogram. Middle panel is the c versus Hubble Residuals relationship, split on the host galaxy stellar mass. High-mass data is presented in filled circle, low-mass data in open circle. High-mass simulations are shown in dashed line, low-mass simulations in dash–dotted line. Bottom panel shows the scatter in the Hubble Residuals, with the same presentation as the middle panel.

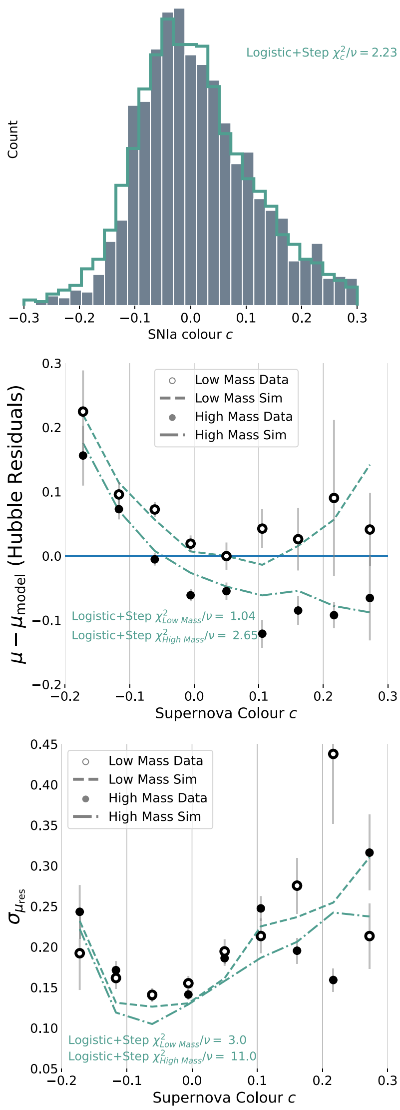

Figure A4. Goodness-of-fit criteria for the Logistic+Step model. Top panel is the colour distribution, with data in grey bars and simulation in solid histogram. Middle panel is the c versus Hubble Residuals relationship, split on the host galaxy stellar mass. High-mass mass data is presented in filled circle, low-mass data in open circle. High-mass simulations are shown in dashed line, low-mass simulations in dash–dotted line. Bottom panel shows the scatter in the Hubble Residuals, with the same presentation as the middle panel.

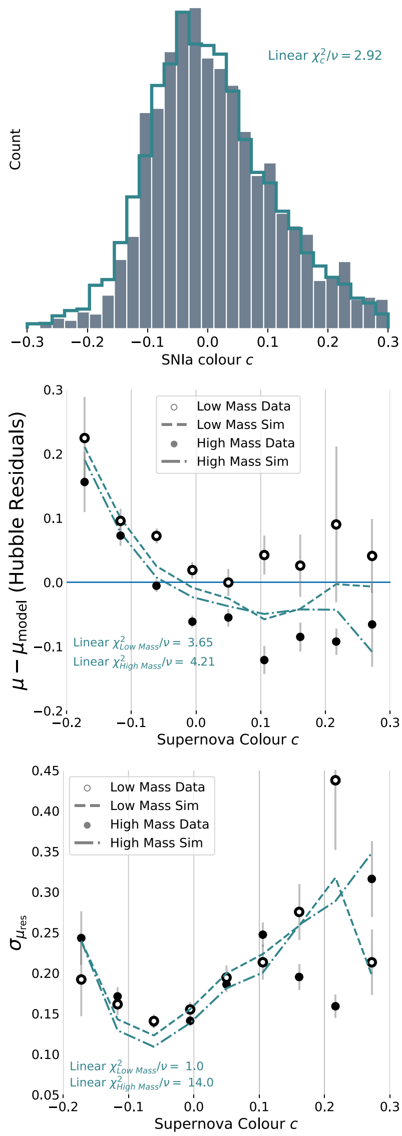

Figure A5. Goodness-of-fit criteria for the Linear model. Top panel is the colour distribution, with data in grey bars and simulation in solid histogram. Middle panel is the c versus Hubble Residuals relationship, split on the host galaxy stellar mass. High-mass data is presented in filled circle, low-mass data in open circle. High-mass simulations are shown in dashed line, low-mass simulations in dash–dotted line. Bottom panel shows the scatter in the Hubble Residuals, with the same presentation as the middle panel.

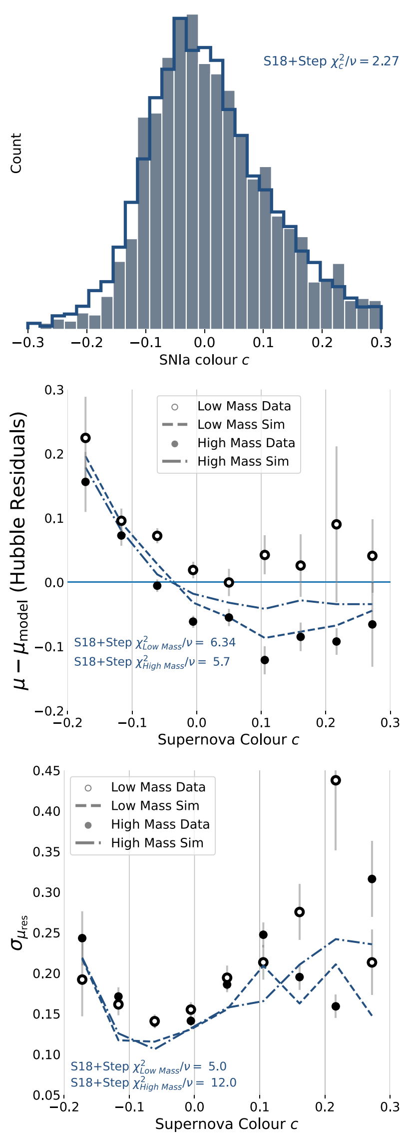

Figure A6. Goodness-of-fit criteria for the S18+Step model. Top panel is the colour distribution, with data in grey bars and simulation in solid histogram. Middle panel is the c versus Hubble Residuals relationship, split on the host galaxy stellar mass. High-mass mass data is presented in filled circle, low-mass data in open circle. High-mass simulations are shown in dashed line, low-mass simulations in dash–dotted line. Bottom panel shows the scatter in the Hubble Residuals, with the same presentation as the middle panel.

[1] *Department of Physics, Duke University Durham, NC 27708, USA*
[2] *School of Physics and Astronomy, University of Southampton, Southampton SO17 1BJ, UK*
[3] *Department of Physics, Lancaster University, Lancs LA1 4YB, UK*
[4] *CENTRA, Instituto Superior Técnico, Universidade de Lisboa, Av. Rovisco Pais 1, P-1049-001 Lisboa, Portugal*
[5] *The Research School of Astronomy and Astrophysics, Australian National University, ACT 2601, Australia*
[6] *Departamento de Física Teórica and IPARCOS, Universidad Complutense de Madrid, E-28040 Madrid, Spain*
[7] *Centre for Astrophysics & Supercomputing, Swinburne University of Technology, Victoria 3122, Australia*
[8] *Departments of Astronomy and Physics, Boston University, Boston, MA 02215, USA*
[9] *INAF-Osservatorio Astronomico di Trieste, via G. B. Tiepolo 11, I-34143 Trieste, Italy*
[10] *Institut d'Estudis Espacials de Catalunya (IEEC), E-08034 Barcelona, Spain*
[11] *Institute of Space Sciences (ICE, CSIC), Campus UAB, Carrer de Can Magrans, s/n, E-08193 Barcelona, Spain*
[12] *Institute of Cosmology and Gravitation, University of Portsmouth, Portsmouth PO1 3FX, UK*
[13] *Department of Astronomy and Astrophysics, University of Chicago, Chicago, IL 60637, USA*
[14] *Kavli Institute for Cosmological Physics, University of Chicago, Chicago, IL 60637, USA*
[15] *Centre for Gravitational Astrophysics, College of Science, The Australian National University, ACT 2601, Australia*
[16] *Department of Physics and Astronomy, University of Pennsylvania, Philadelphia, PA 19104, USA*
[17] *Sydney Institute for Astronomy, School of Physics, A28, The University of Sydney, NSW 2006, Australia*
[18] *School of Mathematics and Physics, University of Surrey, Guildford, Surrey GU2 7XH, UK*
[19] *Aix Marseille Univ, CNRS/IN2P3, CPPM, 13288 Marseille cedex 09, France*
[20] *Cerro Tololo Inter-American Observatory, NSF's National Optical-Infrared Astronomy Research Laboratory, Casilla 603, La Serena, Chile*
[21] *Laboratório Interinstitucional de e-Astronomia – LIneA, Rua Gal. José Cristino 77, Rio de Janeiro, RJ – 20921-400, Brazil*
[22] *Department of Physics & Astronomy, University College London, Gower Street, London WC1E 6BT, UK*
[23] *Kavli Institute for Particle Astrophysics & Cosmology, Stanford University, PO Box 2450, Stanford, CA 94305, USA*
[24] *SLAC National Accelerator Laboratory, Menlo Park, CA 94025, USA*
[25] *Instituto de Astrofisica de Canarias, E-38205 La Laguna, Tenerife, Spain*
[26] *Institut de Física d'Altes Energies (IFAE), The Barcelona Institute of Science and Technology, Campus UAB, E-08193 Bellaterra (Barcelona) Spain*
[27] *Hamburger Sternwarte, Universität Hamburg, Gojenbergsweg 112, D-21029 Hamburg, Germany*
[28] *School of Mathematics and Physics, University of Queensland, Brisbane, QLD 4072, Australia*
[29] *Department of Physics, IIT Hyderabad, Kandi, Telangana 502285, India*
[30] *Jet Propulsion Laboratory, California Institute of Technology, 4800 Oak Grove Dr., Pasadena, CA 91109, USA*
[31] *Institute of Theoretical Astrophysics, University of Oslo. PO Box 1029, Blindern, NO-0315 Oslo, Norway*
[32] *Fermi National Accelerator Laboratory, PO Box 500, Batavia, IL 60510, USA*
[33] *Instituto de Fisica Teorica UAM/CSIC, Universidad Autonoma de Madrid, E-28049 Madrid, Spain*
[34] *Center for Astrophysical Surveys, National Center for Supercomputing Applications, 1205 West Clark St, Urbana, IL 61801, USA*
[35] *Department of Astronomy, University of Illinois at Urbana-Champaign, 1002 W. Green Street, Urbana, IL 61801, USA*
[36] *Santa Cruz Institute for Particle Physics, Santa Cruz, CA 95064, USA*
[37] *Center for Cosmology and Astro-Particle Physics, The Ohio State University, Columbus, OH 43210, USA*
[38] *Department of Physics, The Ohio State University, Columbus, OH 43210, USA*
[39] *Australian Astronomical Optics, Macquarie University, North Ryde, NSW 2113, Australia*
[40] *Lowell Observatory, 1400 Mars Hill Rd, Flagstaff, AZ 86001, USA*
[41] *George P. and Cynthia Woods Mitchell Institute for Fundamental Physics and Astronomy, and Department of Physics and Astronomy, Texas A&M University, College Station, TX 77843, USA*
[42] *LPSC Grenoble - 53, Avenue des Martyrs, F-38026 Grenoble, France*
[43] *Institució Catalana de Recerca i Estudis Avançats, E-08010 Barcelona, Spain*
[44] *Department of Astrophysical Sciences, Princeton University, Peyton Hall, Princeton, NJ 08544, USA*
[45] *Observatório Nacional, Rua Gal. José Cristino 77, Rio de Janeiro, RJ – 20921-400, Brazil*

[46]*Department of Physics, Carnegie Mellon University, Pittsburgh, Pennsylvania 15312, USA*
[47]*Centro de Investigaciones Energéticas, Medioambientales y Tecnológicas (CIEMAT), 28040, Madrid, Spain*
[48]*Department of Physics, University of Michigan, Ann Arbor, MI 48109, USA*
[49]*Computer Science and Mathematics Division, Oak Ridge National Laboratory, Oak Ridge, TN 37831, USA*
[50]*Department of Astronomy, University of California, Berkeley, 501 Campbell Hall, Berkeley, CA 94720, USA*
[51]*Lawrence Berkeley National Laboratory, 1 Cyclotron Road, Berkeley, CA 94720, USA*

This paper has been typeset from a TEX/LATEX file prepared by the author.